Detection of Metallic Objects in Mineralized Soil Using Magnetic Induction Spectroscopy

Wouter van Verre, *Student Member, IEEE*, Liam A. Marsh, *Member, IEEE*, John L. Davidson, Edward Cheadle, Frank J. W. Podd, and Anthony J. Peyton

***Abstract*— The detection of small metallic objects buried in mineralized soil poses a challenge for metal detectors, especially when the response from the metallic objects is orders of magnitude below the response from the soil. This article describes a new, handheld, detector system based on magnetic induction spectroscopy (MIS), which can be used to detect buried metallic objects, even in challenging soil conditions. Experimental results consisting of 1669 passes across either buried objects or empty soil are presented. Fourteen objects were buried at three different depths in three types of soil including nonmineralized and mineralized soils. A novel processing algorithm is proposed to demonstrate how spectroscopy can be used to detect metallic objects in mineralized soils. The algorithm is robust across all types of soil, objects, and depths used in this experiment and achieves a true positive rate over 99% at a false-positive rate of less than 5%, based on just a single pass over the object. It has also been shown that the algorithm does not have to be trained separately for each soil type. The data gathered in the experiment are also published to enable more research on the processing algorithms for MIS-based detectors.**

***Index Terms*— Landmines, magnetic induction spectroscopy, metal detection, mineralized soil, minimum metal, multifrequency.**

I. Introduction

MINERALIZED soils pose a challenge for the detection of buried objects with small metallic contents, such as minimum-metal antipersonnel (AP) landmines, using traditional metal detection. The conductivity and/or permeability of these mineralized soils influence the metal detector in a similar way a metallic object would. Consequently, distinguishing between the mineralized soil and the small metallic objects is difficult; as a result, the rate of false alarms increases in mineralized soils [1]–[3].

Das [4] demonstrated that the magnetic properties of soil can negatively affect the metal detectors, by both masking and altering the signal produced by a buried target. The electromagnetic properties of the soil and the effects on the metal detectors have been widely investigated [5]–[8]—see also [13]–[21] in [4]. Soil-distribution models [7], [8] have been proposed to allow for the simulation of soils with spacial variations and magnetic properties, which may be encountered in the field.

Processing techniques have also been proposed [7], [8] to separate the responses due to magnetic soils and buried metallic objects. In both these cases, the algorithms were developed for the detection of buried unexploded ordnances (UXOs), not minimum-metal AP landmines. These algorithms are also designed for use in postprocessing, requiring the full data set to estimate the power spectral densities of the soil and the buried objects. It was also found that these algorithms are susceptible to errors in the position data associated with the electromagnetic data.

Other models aim to predict the magnetic properties of the soils based on the factors such as rock type, geochemistry, soil age, and annual rainfall [5], and models linking the magnetic properties of the soil and the performance of the metal-detection equipment [6]. While these models provide useful information for the planning stages of demining campaigns, they are not directly applicable to the processing algorithms used in the landmine-detection equipment.

A recent study has shown that the effect of soil mineralization can still be noted when the target objects only contain very small amounts of metal, such as in the case of minimum-metal AP landmines [1]. Therefore, the effect of soil mineralization and the effectiveness of ground compensation are still an important consideration for metal detectors in use in the demining operations [1].

Landmines and other forms of explosive remnants of war pose a lingering threat to communities long after the original conflict is over. In 2017, at least 4795 casualties (deaths and injuries) due to the landmines of all types were recorded, in which 87% were civilians and 47% of those civilian casualties were children [9]. Factory-made AP landmines accounted for at least 748 casualties spread across 23 countries. In the same year, at least 128 km^2 of the previously contaminated land was cleared and at least 168 000 AP landmines were destroyed [9].

As in previous years, landmines remain a serious problem faced by many countries around the world. Metal detection is still the most commonly used tool by the deminers. However, a major difficulty with the clearance of landmines using metal detectors is the false-alarm rate (FAR), which often exceeds 100 false alarms per landmine [10], [11]. This is due to the small amounts of metal present in the modern minimum-metal AP landmines, which is often around 1 g or less [12], and the

Manuscript received June 28, 2019; revised November 18, 2019 and February 9, 2020; accepted March 25, 2020. Date of publication June 9, 2020; date of current version December 24, 2020. This work was supported in part by the Program "SEMIS II" (Scanning Electromagnetic Mine Inspection System) with funding from the charity "Find A Better Way" (www.findabetterway.org.uk) and in part by the Engineering and Physical Sciences Research Council (EPSRC) under Grant EP/N509565/1. *(Corresponding author: Wouter Van Verre.)*

The authors are with the Department of Electrical and Electronic Engineering, The University of Manchester, Manchester M13 9PL, U.K. (e-mail: wouter.vanverre@manchester.ac.uk).

Color versions of one or more of the figures in this article are available online at https://ieeexplore.ieee.org.

Digital Object Identifier 10.1109/TGRS.2020.2994814

presence of metallic clutter in the minefields [10]. As a result, it has been estimated that the cost of landmine clearance falls in the range of 300–1000 USD per landmine [13].

A potential solution to the FAR problem is the use of dual-modality detectors, such as MINEHOUND [14], HSTAMIDS [15], and ALIS [16], which integrate metal detection with the ground-penetrating radar (GPR). With these detectors, it has been demonstrated that it is possible to reduce the rate of false alarms by 77%–95% [14], [16], [17]. Another dual-modality detector system is the Geophex GEM-3M [18], which is based on the Geophex GEM-3 [19] sensor, which is a metal detector based on magnetic induction spectroscopy (MIS).

A new dual-modality detector based on the combination of MIS and GPR, specifically developed for humanitarian demining, is under development at the University of Manchester. Early results of data fusion using both sensor modalities, together with an in-depth description of the overall system, have been reported in previous work [20]. To improve the results of the sensor fusion in the dual-modality detector system, it is first necessary to improve the output from the individual sensor components. Therefore, this article will report solely on the latest progress in the development of the MIS component of this dual-modality system. A novel data-processing algorithm for the detection of metallic objects under adverse soil conditions, which has been tested in multiple soils, will be presented in this article. This algorithm offers good rejection of false alarms due to mineralized soil and can be used in both dual-modality and stand-alone metal detectors. Therefore, this algorithm may be of interest to the wider magnetic induction-sensing community.

II. Background Theory

A metal detector works by generating an ac magnetic field in the area close to the detector. If a metallic object is present inside this primary field, a small secondary magnetic field is generated because of the eddy currents circulating within the object. This secondary field can be measured using a coil, which can be the same coil used to transmit the primary field or a separate coil. If the measured disturbance exceeds a predefined threshold, an alarm can be triggered.

In the pulsed-induction metal detection, a pulse is transmitted and the decay of the pulse is measured. The shape of the decay depends on the secondary magnetic field caused by nearby metallic objects. This broadband time-domain signal can be used to perform target detection and classification by fitting the measured decay against the libraries of the known targets [21], [22].

Alternatively, a frequency-domain approach may be employed using single- or dual-frequency detectors [23], [24]. In these systems, the in-phase and quadrature responses of the object are recorded at a given frequency and used for discrimination purposes. Kruger and Ewalt used phase loops, plotting the in-phase and quadrature components against each other, which are the characteristics of different objects [2], [23].

MIS extends the frequency-domain approach beyond the dual-frequency systems to use multiple excitation frequencies across a wide bandwidth. It has been shown already that MIS can be employed successfully in an industrial setting to classify nonferrous metals in recycling plants [25]. It has also been used to perform measurements of the impedance of biological tissues, for example, to assess the quality of the agricultural produce such as apples, pears, and other fruits [26]. In this biological application, it is possible to place coils around the object, giving multiple simultaneous views of the target. A challenge remains to translate successfully this technology to the handheld systems and buried targets, where the coils of the MIS system are located on only one side of the object [3].

It has previously been shown that, in general, the spectroscopic response of an object depends on its size, conductivity, and permeability [27]. In addition, more specifically, it has been shown previously that landmines have spectroscopic signatures that are distinct from common types of clutter. Different types of landmines also have unique spectra, with distinguishing features, that could be used to discriminate between different mine types [3], [27], [28].

The detector prototype under development at the University of Manchester [28] uses multifrequency excitation to exploit the spectroscopic response of the objects. This technique is known as (electro)magnetic induction spectroscopy (MIS or EMIS). A similar approach has been used by Geophex in their GEM-3 sensor [19], which has been used to characterize the buried UXO [29]. The GEM-3 sensors have also been used to explore the possibility of identifying landmines based on their spectroscopic signature [30].

The work presented in this article builds upon, and extends, the work previously published by the Geophex team. Huang and Won [30] showed that MIS could be applied to the detection of landmines. A digital balancing circuit is added to make better use of the available dynamic range, across a wider band of frequencies. The total signal bandwidth is extended by doubling the maximum frequency in the excitation signal, which is important for soil rejection and the characterization of minimum-metal landmines [30].

The work presented by Huang and Won [29], [30] does not explicitly study the effects of soil mineralization on the performance of the MIS sensor. Soil mineralization is known to have an impact on the performance of the metal detectors [1], [2], and therefore, the spectroscopic response of the soil is analyzed in this article. A novel processing algorithm for the detection of the buried metallic objects is presented here, and the performance is analyzed over three different soil types, including heavily mineralized soil. Furthermore, the MIS sensor formed part of a dual-modality sensor, which creates additional complexity due to the presence of large GPR metallic components in the middle of the coils [31]. The signals captured by the sensor used in this experiment are also being released alongside this article.

III. Materials and Methods

A. MIS Sensor System

A field-deployable, multifrequency MIS system has been developed, consisting of two concentric rings of coils potted within epoxy, which are arranged in a planar configuration.

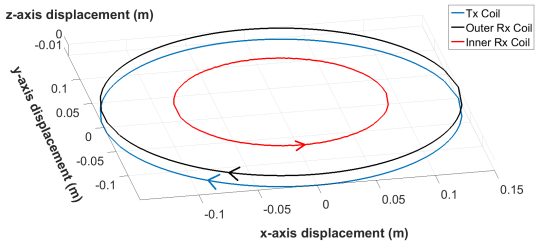

Fig. 1. Geometry of the MIS sensor coils.

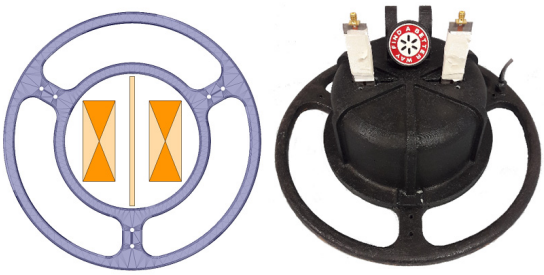

Fig. 2. Geometry of the GPR antennas with respect to the MIS coils shown in the left-hand-side figure. Photograph of the combined sensor head shown on the right-hand side.

The transmit and receive coils are encapsulated inside the epoxy for increased rigidity and durability. The transmit coil is placed in the outer ring, while the receiver coil is split into two components that are placed in both the outer and inner rings. The geometry is shown in Fig. 1.

The spectroscopic metal detector described here is part of a dual-modality detector system, integrating MIS with GPR. The antennas for the GPR system are placed inside the inner receiver coil, as shown in Fig. 2. The GPR feed structure and backing foam (radar-absorbing foam) are placed inside a 3-D printed structure that covers the inner receiver coil. A photograph of the combined MIS–GPR sensor head is also shown in Fig. 2.

The MIS system reported here uses a receiver-bucked configuration, so the two parts of the receive coil are connected in series opposition such that the net induced voltage on the receive coil is as close to zero as possible in free space, and the turns ratio of the two parts of the receive coil is chosen to aid in this. The position of the coils inside the sensor head is designed to achieve the best possible null in the system. In practice, it is difficult to achieve a perfect null across a wide range of frequencies, because the two elements of the receiver coil have different transimpedance characteristics with respect to the transmitter coil. As a result, it is difficult to achieve a perfect subtraction of these two coil elements.

To improve the balance between the coils and move the net induced voltage closer to zero, an electronic nulling signal can be injected into the receiver signal conditioning chain to remove any induced signal that could not be removed using the inductive balancing. Furthermore, this final step can also be used to subtract the influence of the metallic components near the MIS coils, such as mounting hardware and printed-circuit boards with the first-stage amplifiers. This is especially useful when developing a dual-modality detector system, as the integration of the GPR component necessitates the introduction of the metallic components, such as antennas and feed cables, near the MIS coils.

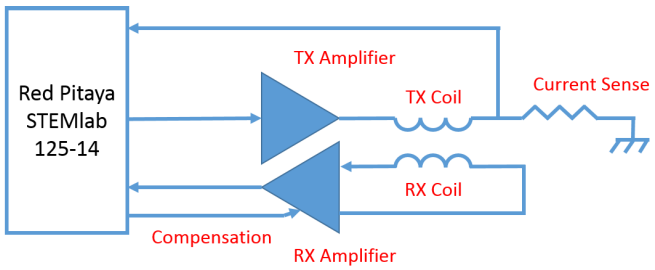

Fig. 3. High-level block diagram of the MIS electronics.

The electronics in the MIS system have been developed around the Red Pitaya STEMlab 125-14 and are capable of measuring up to 16 frequencies simultaneously. The exact frequency content of the transmitted signal can be varied, which allows fine control over both the relative phase and magnitudes of the individual harmonics. The electronics provide two high-speed (125 MSPS) input channels and two high-speed (125 MSPS) output channels, both of which are 14 bits wide. The two input channels are used to measure the voltage across the receive coil and the current through the transmit coil, respectively. The first output channel is used to drive the transmit coil, while the second channel is used to generate the electronic nulling signal described previously. A block diagram of the MIS electronics system is shown in Fig. 3. After digital signal processing on the system-on-chip, the final output sample rate of the demodulated transimpedance values is approximately 120 Hz. Each of the components in the output data is 22-bit-wide signed integers and is sign-extended to 32 bits for ease of use.

The phase and quadrature-phase components of the MIS response are calibrated using a small piece of ferrite. Complex calibration factors are calculated such that the response of the ferrite at a distance of 7 cm has a unit magnitude along the in-phase axis. The ferrite piece is a cylindrical piece of type 4B1 Ferroxcube with a length of 16 mm and a diameter of 5 mm.

B. Position Tracking

A machine-vision-based tracking system has been developed to log the position of the sensor head, as it is moved over the ground. This system can be used to validate the response of the MIS system by comparing the position of the sensor response with the known position of the buried object(s), thus improving the confidence that the sensor response corresponds to the real objects. In future, the position-tracking system may also be used to improve the data-processing algorithms. The tracking system is based on a universal serial bus (USB) camera system, through which the sample rates of 30–50 Hz can be achieved using a 1280×1024 pixel image resolution.

A small printed chessboard sheet is mounted on the top of the sensor head and the camera is placed on a tripod to the side of the test area. The position of the sensor head is determined

(a)

(b)

(c)

Fig. 4. Test objects used during the trial. (a) PMA3 (left) and PMA2 (right) landmines. (b) Metallic objects. (c) Nonmetallic objects.

from the position of the chessboard sheet in the camera image using OpenCV [32] and the known pose of the camera with respect to the test lane. The pose of the camera is determined separately by calibration.

C. Experimental Methodology

The experiment described in this article was carried out in May 2018 in Benkovac, Croatia, at a test site run by HCR-CTRO. A set of objects consisting of different metallic objects, or objects with metallic components, as well as common nonmetallic clutter objects, was chosen to cover a range of object shapes, sizes, and materials. The spectroscopic response of these objects was first measured in air, and subsequently, the objects were buried in soil. The objects were buried at the end of the test lanes, and the ground was not specially prepared or flattened. Therefore, the surface roughness is typical of that found at the Benkovac testing facility.

Two minimum-metal landmines were used: PMA3 and PMA2 [shown in Fig. 4(a)]. The other items were a 12-mm ball bearing, a 10 Eurocent coin, an approximately 80-mm-long bullet and casing, the tail of a mortar bomb, a 55-mm-long bullet and casing, a ring pull from a drinks can, and a 1 Euro coin. These objects are shown in Fig. 4(b). Finally, four nonmetallic objects were also buried. These consisted of two rocks and two wooden cylinders, as shown in Fig. 4(c).

TABLE I

SUSCEPTIBILITY VALUES OF THE SOIL TYPES IN BENKOVAC; VALUES ARE TAKEN FROM [33]

Soil Type	Susceptibility at 958 Hz (SI)	Susceptibility Difference at 465 Hz and 4650 Hz (SI)
"Cooperative"	$(13 \pm 2) \times 10^{-5}$	0.6×10^{-5}
"Uncooperative"	$(154 \pm 13) \times 10^{-5}$	25.5×10^{-5}
"Rocky"	$(190 \pm 36) \times 10^{-5}$	35.4×10^{-5}

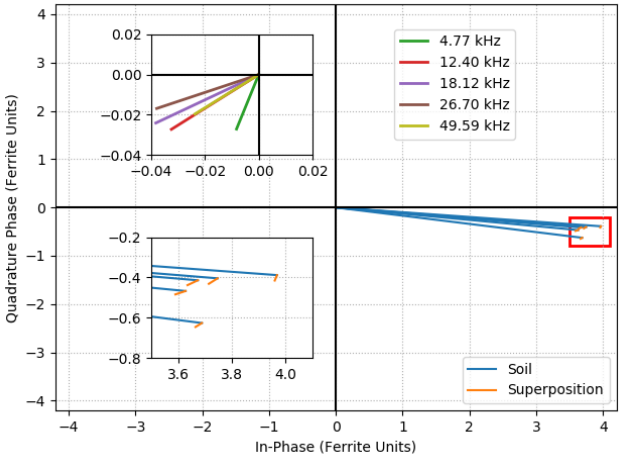

Fig. 5. Illustrative example of the comparison between the soil spectrum and a landmine signature.

There are three types of soil available at the test location in Benkovac: a homogeneous mineralized soil (labeled "Uncooperative"), a homogeneous nonmineralized soil ("Cooperative"), and a heterogeneous mineralized soil ("Rocky"). The susceptibility values of these types of soil were measured by Mueller *et al.* [33] and are repeated in Table I. Each object was buried at three depths (flush, 5 and 10 cm; measured to the top of the objects) in each of the three types of soil.

Fig. 5 shows an illustrative example, demonstrating the highly uncooperative nature of the mineralized soil in Benkovac. In the bottom quadrants of Fig. 5, the average spectrum from the uncooperative ground is shown in blue. The spectrum of the PMA2 landmine, measured in air (7.5-cm distance), is shown in orange, added on the top of the soil spectrum. The inset image shows a close-up of the end of the vectors. The second inset image shows the spectrum of the PMA2 landmine. It can be seen that the spectrum of the landmine is significantly smaller than that of the uncooperative soil. These frequencies were chosen to capture the typical response curves from the AP landmines, based on prior work [20], [27].

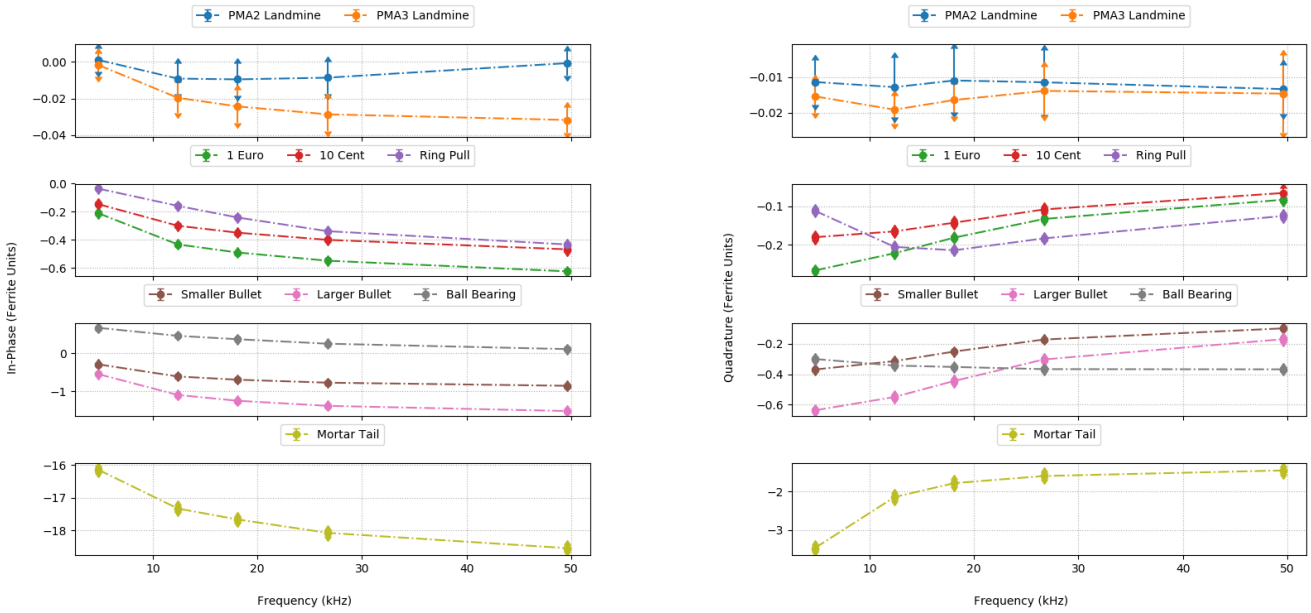

Fig. 6. Spectra of the objects, as measured in air, at a distance of 7.5 cm. Error bars indicate one standard deviation. (a) In-phase component. (b) Quadrature component.

For each of these test conditions, the handheld sensor was swept across the buried objects and results were recorded for further processing. At least 12 passes over the object were recorded for each of the test conditions.

Due to the presence of large rocks in the "Rocky" soil, similar in shape and color to one of the test rocks, it was decided not to bury this rock at a depth of 10 cm in the "Rocky" soil. The concern was that it would not be possible to locate the rock again afterward for testing in the other soils.

IV. Results

A. Spectroscopy Measurements

Fig. 6(a) and (b) shows the result of the experiment, where the objects were measured in front of the detector, at a distance of 7.5 cm. This distance corresponds approximately to the distance between an object buried at 5-cm depth and the detector, once the liftoff of the sensor head over the ground is considered. It should be noted that the quadrature components of the response of the landmines should tend to zero for the highest frequencies. There is a small deviation from this pattern in the spectra shown here, which falls within the standard deviation of the measurements. This is likely due to noise in either the object or the calibration measurement [20]. The objects are grouped together based on the magnitudes of their spectra. The magnitude of the spectra of the landmine is at least an order of magnitude smaller than that of the coins, the ring pull, and the ball bearing. The spectra of the bullets are approximately double in magnitude compared with those objects, and the spectrum of the mortar tail is another order of magnitude larger.

Fig. 7(a) and (b) shows the in-phase and quadrature components of the three different types of soil used in this experiment, as measured by the experimental MIS sensor. The magnitude of the response from the uncooperative soil is approximately double that of the magnitude of the response from the large metallic objects such as the bullets and the ball bearing. This is more than two orders of magnitude larger than the response from the PMA2 and PMA3 landmines at 7.5-cm distance.

B. Signal Preprocessing

A first-order model of the signals received from the metal detector can be constructed by considering the measurements to be a superposition of the background coupling between the coils, the response of the soil, the drift in the system, and the noise in the system. If an object is buried near the detector, its response would also form part of the superposition. This superposition is shown in the following equation:

$$\vec{\boldsymbol{x}}[n] = \vec{\boldsymbol{b}} + \vec{\boldsymbol{s}}[n] + \vec{\boldsymbol{o}}[n] + \vec{\boldsymbol{v}}[n] + \vec{\boldsymbol{w}}[n]. \tag{1}$$

Here, $n = 0, 1, \ldots, N-1$ corresponds to the N discrete-time samples collected during the scan, where $\vec{\boldsymbol{x}}[n] = [x_1[n], \ldots, x_k[n]]^T$ is a vector representing the measured signal at sample n, at each of the K harmonics $h_1, \ldots, h_k$ of interest, and $\vec{\boldsymbol{b}} = [b_1, \ldots, b_k]^T$ the time-invariant background residual coupling, $\vec{\boldsymbol{s}}[n] = [s_1[n], \ldots, s_k[n]]^T$ the signal from the soil underneath the sensor at time t, and $\vec{\boldsymbol{v}}[n] = [v_1[n], \ldots, v_k[n]]^T$ and $\vec{\boldsymbol{w}}[n] = [w_1[n], \ldots, w_k[n]]^T$ represent the drift and the noise in the system, respectively. Finally, the object response $\vec{\boldsymbol{o}}[n]$ is described as $\vec{\boldsymbol{o}}[n] = [o_1[n], \ldots, o_k[n]]^T$, where $\vec{\boldsymbol{o}}[n] = [0, \ldots, 0]^T$ when no object is present. All of these vectors are complex-valued.

In practice, the drift in the system, $\vec{\boldsymbol{v}}[n]$, occurs primarily due to a change in the residual coupling signal b due to

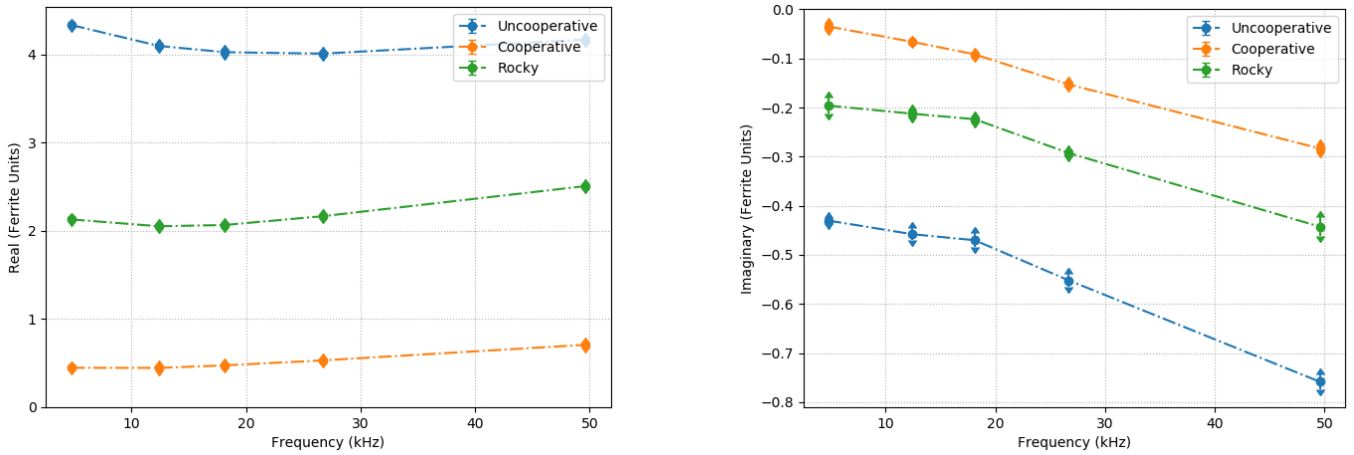

(a) (b)

Fig. 7. Spectra of soils, measured approximately 2–3 cm away. Mean of 0.5 s of data. Error bars indicate one standard deviation. (a) In-phase component. (b) Quadrature component.

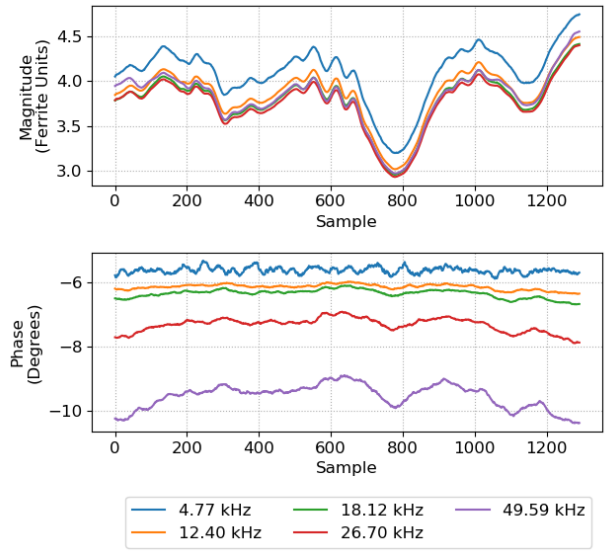

Fig. 8. Magnitude and phase response of the mineralized soil—no object present.

the changes in the temperature of the sensor, which cause expansion and contraction of the coils. Therefore, these two signals can be considered as a single time-varying background coupling signal $b[n]$. This leads to a simplification of the superposition, as shown in the following equation:

$$\vec{\boldsymbol{x}}[n] = \vec{\boldsymbol{b}}[n] + \vec{s}[n] + \vec{o}[n] + \vec{w}[n]. \tag{2}$$

Fig. 8 shows the magnitude and phase of the measured signals at all frequencies from a scan over empty, mineralized, soil. From these data, it can be seen that the soil response is not constant across a scan. However, most of the soil variation is due to changes in magnitude, which varies at least ±20%, while the phase angle of the response stays mostly constant, varying less than ±1% across all samples. The changes in magnitude are likely due to the changes in the distance between the sensor head and the ground due to the surface undulation and movement by the operator. Another reason could be due to the changes in the local mineral content of the soil.

A detection algorithm can be applied to the raw data to determine the likelihood of an object being present. A number of assumptions are made to simplify the processing algorithm.

1) The phase response of the spectrum of the soil stays the same throughout the scan, so that $\angle\vec{s}[n] = \vec{\alpha}[n] = \vec{\alpha}$.
2) An assumption is made that $\vec{\boldsymbol{b}}[0] = 0$ and that the drift is slow, so that it can be ignored for small values of n.
3) It is assumed that there are no objects under the detector at the start of each scan, so that $\vec{o}[0] = 0$; this is guaranteed through the experimental procedure.

Using these assumptions, the algorithm works as follows: first, a 20-point moving average filter (corresponding to approximately 0.1667 s) is applied to the time sequence $\vec{\boldsymbol{x}}[n]$ to smooth the measurements. Next, the phase response of the spectrum of the soil, $\vec{\boldsymbol{\alpha}}$, is estimated using the mean of the initial data. Since $\vec{\boldsymbol{x}}[n]$ is complex-valued, let $\vec{\boldsymbol{x}}[n] = \vec{\boldsymbol{X}}[n] + j\vec{\boldsymbol{Y}}[n]$. Then, $\vec{\boldsymbol{\alpha}}$ is

$$\vec{\boldsymbol{\alpha}} = \angle\vec{s} = \arctan\left(\frac{\sum_{i=0}^{M} \frac{\vec{Y}[i]}{M}}{\sum_{i=0}^{M} \frac{\vec{X}[i]}{M}}\right) \tag{3}$$

where $M = 60$, corresponding to half a second of data. The complex-valued points at each time step in the sequence $x[n]$ are then rotated such that the ground response is entirely in-phase

$$\vec{\boldsymbol{x}}_{\boldsymbol{r}}[n] = \vec{\boldsymbol{x}}[n]e^{-j\vec{\boldsymbol{\alpha}}}. \tag{4}$$

It can be seen that the rotated signal $\vec{\boldsymbol{x}}_{\boldsymbol{r}}[n]$ will contain a rotated view of the spectrum of the object $\vec{o}[n]$. In the case of object detection, this is not an issue, since there is no attempt being made in this article to identify or recognize the spectra of the objects.

The next step of the preprocessing algorithm is to extract the quadrature, or imaginary, component of each element in $\vec{\boldsymbol{x}}[\boldsymbol{n}]$.

This step essentially removes the ground response, $\vec{s}$, from the signal, due to the rotation performed previously

$$\begin{aligned}\vec{z}[n] &= \mathrm{Im}(\vec{x_r}[n]) \\ &= \sin(\vec{\gamma}[n] - \vec{\alpha})|o[n]| \\ &\quad + \sin(\vec{\beta}[n] - \vec{\alpha})|b[n]| + \vec{w'}[n] \end{aligned} \tag{5}$$

where $w'[n] = \mathrm{Im}(\vec{w}[n])$, $\vec{\beta}[n] = \angle\vec{b}[n]$, and $\gamma[n] = \angle\vec{o}[n]$. It can be seen that $\boldsymbol{z[\vec{n}]}$ contains the projection of $\vec{o}[n]$ and $\vec{b}[n]$ onto the axis perpendicular to the soil spectrum $\vec{s}$. An unfortunate side effect of this processing step is that any part of the object response along the axis of the soil spectrum is disregarded. The background signal $\boldsymbol{b[\vec{n}]}$ varies slowly compared with the object signal $\vec{o}[n]$, when an object is within the sensitive region of the sensor. Therefore, the projection of $\boldsymbol{b[\vec{n}]}$ can be removed using a high-pass filter. This high-pass filter is implemented by subtracting the output of a long moving average (300 points, corresponding to 2.5 s), which is easily implemented in an embedded system.

C. Real-Time Object Detection

For object detection, the feature vector $\vec{z}[n]$ is reduced to a single scalar corresponding to the likelihood (λ) that a metallic object is present. The real-time object-detection algorithm performs a weighted sum, as shown in the following equation:

$$\lambda[n] = \sum_{k=0}^{k=K} |z_k[n]|^a * w_k. \tag{6}$$

This algorithm can also be viewed as a modification on the traditional linear-regression model. In this case, the elements of $\vec{z}[n]$ are first raised to the power of a. This either reduces or magnifies the effect of large variations in $z_i[n]$, depending on whether $a < 1$ or $a > 1$, respectively.

The coefficient a and weights w_i were optimized using the *differential evolution* strategy in *SciPy* [34], [35]. The goal function for the optimizer was to minimize the area outside of the receiver operating characteristic (ROC) curve or, in other words, to maximize the area under the ROC curve. For the calculation of the true-positive rate, only positive detection in the vicinity of the buried targets is considered, while the false-positive rate is calculated based on the scans containing no object or a nonmetallic object.

Binary classification is performed using the following equation:

$$\vec{y_p}[n] = \begin{cases} 0, & \text{if } x < T \\ 1, & \text{if } x \geq T \end{cases} \tag{7}$$

where $\vec{y_p}$ is the predicted set of labels and T is the threshold. Label 0 corresponds to no metal being present and label 1 corresponds to metal being present. The ROC curves are computed by varying the value of T.

An example of the optimal values found using this approach is

$$a = 0.5270363$$

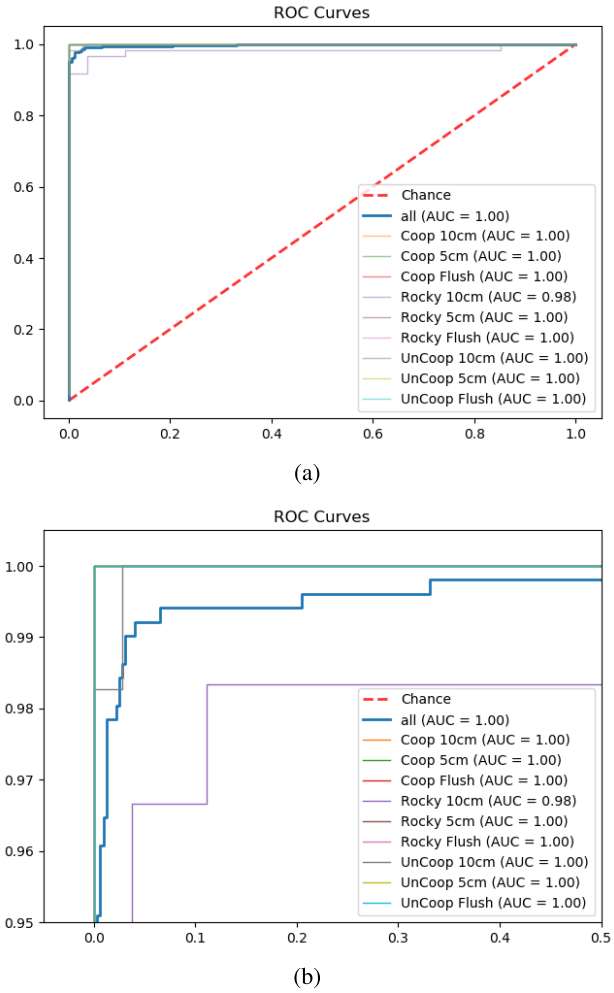

Fig. 9. Family of ROC curves showing the performance across all data sets and the individual combinations of soil type and depth. (a) Full ROC curves. (b) Close look at the top-left corner of the ROC curve.

and

$$\vec{w} = \begin{bmatrix} 0.1128332 \\ 3.0140624 \\ 1.3885450 \\ -1.4922703 \\ -0.1157962 \end{bmatrix}.$$

The ROC curves can be calculated by characterizing each scan in the data set based on the values of $\lambda[n]$. The data set was divided into a training set used to optimize a and $\vec{w}$, and a test set used for calculating the ROC curves.

The ROC curves can be calculated separately for each combination of soil and depth, which means there will be different thresholds for each soil and depth. Alternatively, the ROC curve can be computed for the entire test data set at once, corresponding to a single, global, threshold used across all soil types and depths. Fig. 9(a) shows the resulting ROC curves for individual soils and depths, and one curve using all data at once. Fig. 9(b) shows a close-up of the top-left corner of the plot.

It can be seen that the algorithm works as a perfect classifier for all three soils for the depths of 0 and 5 cm. For a depth of 10 cm, the classifier is no longer perfect; however,

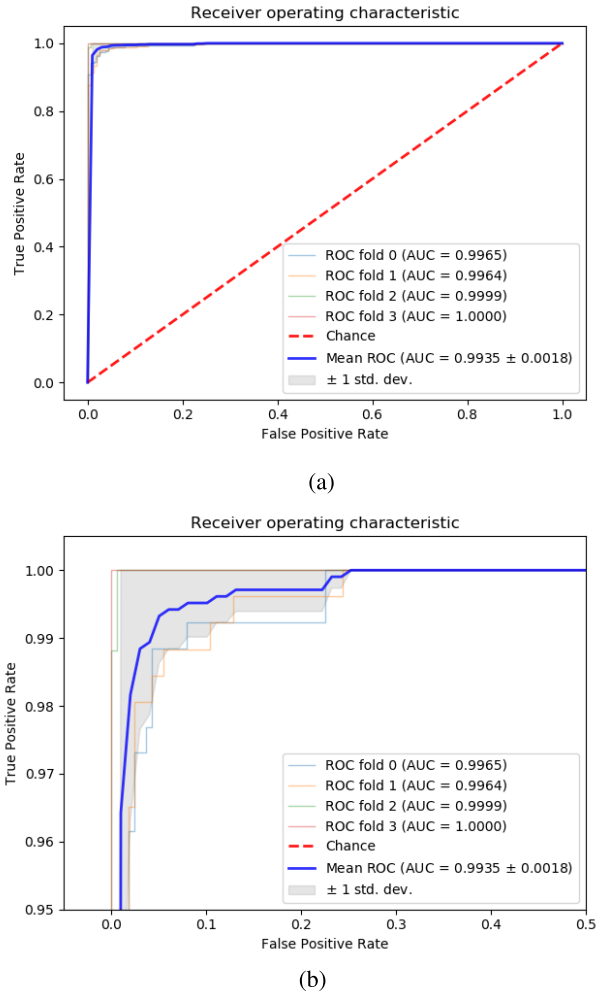

Fig. 10. ROC curve with cross-validation using fivefolds. (a) Full ROC curve, with the mean and individual folds shown. (b) Close look at the top-left corner of the ROC curve.

the algorithm still performs well. It can also be seen that using a single, global, threshold results in a good performance as well.

To ensure that the algorithm is robust with respect the choice of test and training data, another family of ROC curves was constructed using cross-validation. In this test, the ROC curves are computed using a single threshold across all combinations of depth and soil. The Stratified K-Fold algorithm from *scikit-learn* [36] was used for cross-validation purposes.

This algorithm divides the full data set into k subsets. The assignment of samples into the subsets is done randomly, but in such a way that each subset is the representative of the original data set. All but one of the subsets is then used to train the model, in this case by optimizing the values of a and w, and the final subset is used to validate the model by calculating the ROC curve. This process is repeated until every subset has been used once to validate the model.

At this point, care must be taken that the subsets are truly representative of the whole data set. In this study, the data are divided into two classes: *no metal* and *metal*. However, the samples in these classes can be further divided into subclasses. For the *no-metal* class, the subclasses are empty scans and the four nonmetallic objects, while the *metal* class contains subclasses for each of the metallic objects.

If the Stratified K-Fold algorithm is applied using the two-class model, it is possible that the subsets become skewed. For example, one subset may contain the correct number of samples from the *metal* class, but all these samples could be coins; or all of the *metal* class samples might be small objects, such as the PMA2 and PMA3 landmines. This kind of skew could cause a potential problem when evaluating the results of cross-validation.

To avoid this problem, the data set is labeled twice. The first set of labels uses the two-class model (*metal* and *no metal*), while the second set of labels uses 14 classes (one for each object type). The second set of labels is used only for the Stratified K-Fold algorithm to ensure that the subsets are truly representative of the source data set. The first set of labels is subsequently used for both training and validation.

Fig. 10(a) shows the ROC curve for each fold from the Stratified K-Fold algorithm (with fivefolds), as well as the mean ROC curve and the standard deviation of the ROC curve. Fig. 10(b) shows the top-left corner in more detail. These figures show that the algorithm is robust to different selections of the training and testing data. The mean ROC curve in Fig. 10(a) shows that the proposed algorithm achieves a true-positive rate of over 95% with a false-positive rate of less than 1%, across a range of soils and target depths. A true-positive rate of 99% is achieved with a false-positive rate of less than 5%. This is using just a single pass over the buried object. In practice, it is likely that the operator would use multiple passes over an object to discount spurious false alarms and improve the probability of detection for a given FAR.

V. Conclusion

A new MIS metal-detector system, which is part of a wider project to develop a new dual-modality landmine detector, has been introduced. The system is receiver-bucked and uses inductive and active balancing to minimize the net induced voltage in free space. The active balancing is also used to subtract the response from the GPR components near the coils, such as the antennas. It has been shown the MIS detector can be used successfully to detect metallic objects, including small quantities of metal such as those found in the minimum-metal AP landmines. MIS can be used even in heavily mineralized, highly uncooperative soils, where the mineral content in the ground can increase the rate of false alarms. These experiments were performed alongside the GPR component of the dual-modality detector, showing that the presence of the GPR does not compromise the MIS performance.

The response of mineralized has been investigated, and it has been shown that the magnitude of the soil response is at least two orders of magnitude greater than that of the minimum-metal AP landmines at moderate depths (5 cm). Furthermore, it was shown that the magnitude of the soil response can vary significantly (at least $\pm 20\%$) due to the local soil conditions and changes in the sensor liftoff, as the sensor is swept over the ground. As a consequence, the changes in soil response are much larger than the response of the buried objects.

The analysis of the soil response also revealed that variation in the soil response is largely in the magnitude of the spectrum, while the phase angles of the spectrum remain broadly constant, as the sensor is moved across the soil. This finding can be exploited by processing algorithms to improve the rejection of false alarms due to soil features.

In this article, a novel algorithm for processing MIS data has been presented based on extracting the part of the object response that is perpendicular to the soil response. This makes the algorithm less responsive to variations in the soil profile, which can have magnitudes 10–100 times larger than that of the target response. The proposed algorithm works well for all soil conditions and targets used in this experiment, and achieves a rate of true positives of 99% with an FAR of less than 5%, with only a single pass over a buried object. The prototype detector, with the proposed algorithm, can perfectly detect all objects in this data set buried at 5 cm or less. The algorithm did not have to be trained separately for each soil type.

Research on processing algorithms for MIS data has been limited in the past, at least partly due to the difficulty with accessing handheld MIS detector systems. Therefore, the measurements taken during this experiment are being made publicly available to aid in the development of processing algorithms for metal detection and characterization systems by other groups.

VI. Data Set

The data set described here is published alongside this article, through IEEE DataPort (DOI: 10.21227/dr68-9t61), to encourage the further development of the processing algorithms by third parties. Every sweep over an object is contained in a different file, with the following file-naming convention being used: *<ID>_<Soil Type>_<Object Depth>_<Object>.h5*, where *<ID>* is the globally unique identifier for the file.

Each file is an HDF5 file generated using *Pandas* [37], containing a single DataFrame. The DataFrame contains eight columns. The first three correspond to the x-, y-, and z-positions (in cm) relative to the arbitrary data.

The arbitrary data stay constant for all sweeps over all objects in a given combination of soil and depth. The other five columns contain the complex transimpedance values as measured by the MIS system, after calibration against the ferrite piece.

As explained in the main body, there are no data for one of the rocks buried at 10-cm depth in "Rocky" soil.

Acknowledgment

The authors would like to thank HCR-CTRO for the access to the test site in Benkovac, Croatia.

References

[1] K. Takahashi, H. Preetz, and J. Igel, "Soil properties and performance of landmine detection by metal detector and ground-penetrating radar—Soil characterisation and its verification by a field test," *J. Appl. Geophys.*, vol. 73, no. 4, pp. 368–377, Apr. 2011.

[2] H. Krüger and H. Ewald, "Signal processing and pattern recognition for eddy current sensors, used for effective land-mine detection," in *Autonomous and Intelligent Systems*, M. Kamel, F. Karray, W. Gueaieb, and A. Khamis, Eds. Berlin, Heidelberg: Springer, 2011, pp. 294–302.

[3] I. J. Won, D. Keiswetter, and T. H. Bell, "Electromagnetic induction spectroscopy for clearing landmines," *IEEE Trans. Geosci. Remote Sens.*, vol. 39, no. 4, pp. 703–709, Apr. 2001.

[4] Y. Das, "Effects of soil electromagnetic properties on metal detectors," *IEEE Trans. Geosci. Remote Sens.*, vol. 44, no. 6, pp. 1444–1453, Jun. 2006.

[5] R. L. van Dam, J. M. H. Hendrickx, J. B. J. Harrison, and B. Borchers, "Conceptual model for prediction of magnetic properties in tropical soils," *Proc. SPIE*, vol. 5794, no. 1, p. 177, 2005.

[6] J. Igel, H. Preetz, and S. Altfelder, "Magnetic viscosity of tropical soils: Classification and prediction as an aid for landmine detection," *Geophys. J. Int.*, vol. 190, no. 2, pp. 843–855, Aug. 2012.

[7] L. R. Pasion, S. D. Billings, and D. W. Oldenburg, "Evaluating the effects of magnetic susceptibility in UXO discrimination problems," SERDP SEED Project, Alexandria, VA, USA, Tech. Rep. MR-1285, 2002.

[8] Y. Li *et al.*, "Final report improving UXO detection and discrimination in magnetic environments," SERDP, Alexandria, VA, USA, Tech. Rep. MR-1414, May 2010.

[9] ICBL. (2018). *Landmine Monitor 2018*. [Online]. Available: https://www.the-monitor.org/cp

[10] UN. Secretary-General, "Assistance in mine clearance: Report of the secretary-general (A/49/357)," Secretary-Gen. United Nations, New York, NY, USA, Tech. Rep. (A/49/357), 1994.

[11] D. J. Daniels, "A review of GPR for landmine detection," *Sens. Imag., Int. J.*, vol. 7, no. 3, pp. 90–123, Sep. 2006.

[12] C. King, *Jane's Mines and Mine Clearance*, C. King, Ed. 16th ed. London, U.K.: Jane's Information Group, 2011.

[13] E. N. Walsh and S. W. Walsh, "Rehabilitation of landmine victims—The ultimate challenge," World Health Organisation, Geneva, Switzerland, Tech. Rep. 03, 2003. [Online]. Available: https://www.who.int/bulletin/volumes/81/9/Walsh.pdf

[14] D. Daniels, J. Braustein, and M. Nevard, "Using minehound in Cambodia and Afghanistan," *J. ERW Mine Action*, vol. 18, no. 2, pp. 1–5, 2014.

[15] C. Amazeen and M. Locke, "Developmental status of the U.S. Army's new handheld standoff mine detection system (HSTAMIDS)," in *Proc. 2nd Int. Conf. Detection Abandoned Land Mines*, 1998, pp. 193–197.

[16] M. Sato, K. Kikuta, and I. Chernyak, "Dual sensor, 'ALIS' for humanitarian demining," in *Proc. 17th Int. Conf. Ground Penetrating Radar (GPR)*, Jun. 2018, pp. 1–4.

[17] The Halo Trust. (2011). *Halo Utilises Dual-Sensor DeteCTOR | The Halo TrusT*. [Online]. Available: https://www.halotrust.org/media-centre/news/halo-utilises-dualsensor-detector/

[18] Geophex Ltd., "GEM-3M: A ground imager with a local navigator," Geophex, Raleigh, NC, USA, Tech. Rep., 2012.

[19] I. J. Won, D. Keiswetter, D. R. Hanson, E. Novikova, and T. M. Hall, "GEM-3: A monostatic broadband electromagnetic induction sensor," *J. Environ. Eng. Geophys.*, vol. 2, no. 1, pp. 53–64, 1997.

[20] L. A. Marsh *et al.*, "Combining electromagnetic spectroscopy and ground-penetrating radar for the detection of anti-personnel landmines," *Sensors*, vol. 19, no. 15, p. 3390, Aug. 2019.

[21] S. L. Tantum and L. M. Collins, "A comparison of algorithms for subsurface target detection and identification using time-domain electromagnetic induction data," *IEEE Trans. Geosci. Remote Sens.*, vol. 39, no. 6, pp. 1299–1306, Jun. 2001.

[22] C. V. Nelson, C. B. Cooperman, W. Schneider, D. S. Wenstrand, and D. G. Smith, "Wide bandwidth time-domain electromagnetic sensor for metal target classification," *IEEE Trans. Geosci. Remote Sens.*, vol. 39, no. 6, pp. 1129–1138, Jun. 2001.

[23] H. Krüger and H. Ewald, "Handheld metal detector with online visualisation and classification for the humanitarian mine clearance," in *Proc. IEEE Sensors*, Oct. 2008, pp. 415–418.

[24] C. Bruschini and H. Sahli, "Phase angle based clutter reduction and 2D Imaging using data from a commercial differential two frequency EMI system," *Proc. SPIE*, vol. 4038, pp. 24–28, Apr. 2000.

[25] M. D. O'Toole, L. A. Marsh, J. L. Davidson, Y. M. Tan, D. W. Armitage, and A. J. Peyton, "Non-contact multi-frequency magnetic induction spectroscopy system for industrial-scale bio-impedance measurement," *Meas. Sci. Technol.*, vol. 26, no. 3, Mar. 2015, Art. no. 035102.

[26] M. D. O'Toole, N. Karimian, and A. J. Peyton, "Classification of nonferrous metals using magnetic induction spectroscopy," *IEEE Trans. Ind. Informat.*, vol. 14, no. 8, pp. 3477–3485, Aug. 2018.

[27] O. A. Abdel-Rehim, J. L. Davidson, L. A. Marsh, M. D. O'Toole, and A. J. Peyton, "Magnetic polarizability tensor spectroscopy for low metal anti-personnel mine surrogates," *IEEE Sensors J.*, vol. 16, no. 10, pp. 3775–3783, May 2016.
[28] L. A. Marsh *et al.*, "Spectroscopic identification of anti-personnel mine surrogates from planar sensor measurements," in *Proc. IEEE Sensors*, Oct./Nov. 2016, pp. 1–3.
[29] H. Huang and I. J. Won, "Characterization of UXO-like targets using broadband electromagnetic induction sensors," *IEEE Trans. Geosci. Remote Sens.*, vol. 41, no. 3, pp. 652–663, Mar. 2003.
[30] H. Huang and I. J. Won, "Automated identification of buried landmines using normalized electromagnetic induction spectroscopy," *IEEE Trans. Geosci. Remote Sens.*, vol. 41, no. 3, pp. 640–651, Mar. 2003.
[31] W. van Verre, X. Gao, F. J. Podd, D. J. Daniels, and A. J. Peyton, "GPR bowtie antennas with reduced induction footprints for dual-modality detectors," in *Proc. IEEE Int. Symp. Antennas Propag. USNC-URSI Radio Sci. Meeting*, Jul. 2019, pp. 600–859.
[32] G. Bradski, "The openCV library," *Dr. Dobb's J. Softw. Tools*, vol. 25, pp. 120–125, Nov. 2000.
[33] C. Mueller *et al.*, "Reliability model for test and evaluation of metal detectors," Federal Inst. Mater. Res. Test. (BAM), Berlin, Germany, Tech. Rep. ITEP Project 2.1.1.2, Sep. 2004.
[34] E. Jones, T. Oliphant, and P. Peterson. *SciPy: Open Source Scientific Tools for Python*. Accessed: Jun. 5, 2019. [Online]. Available: http://www.scipy.org/
[35] R. Storn and K. Price, "Differential evolution–A simple and efficient heuristic for global optimization over continuous spaces," *J. Global Optim.*, vol. 11, no. 4, pp. 341–359, 1997.
[36] F. Pedregosa *et al.*, "Scikit-learn: Machine learning in Python," *J. Mach. Learn. Res.*, vol. 12, pp. 2825–2830, Oct. 2011.
[37] W. McKinney, "Data structures for statistical computing in python," in *Proc. 9th Python Sci. Conf.*, S. van der Walt and J. Millman, Eds. 2010, pp. 51–56.

Wouter van Verre (Student Member, IEEE) received the B.Eng. (Hons.) degree in electrical and electronics engineering from The University of Manchester, Manchester, U.K., in 2016, where he is pursuing the Ph.D. degree in the use of electromagnetic methods for the detection of buried landmines. His research interests include the use of metal detection in polar environments and multi-in–multiout (MIMO) ground-penetrating radar.

Liam A. Marsh (Member, IEEE) received the M.Eng. (Hons.) degree in electrical engineering and electronics from the Institute of Science and Technology, University of Manchester, Manchester, U.K., in 2007, and the Ph.D. degree in electromagnetic tomography and people screening from The University of Manchester in 2011.

He subsequently joined the Sensing, Imaging and Signal Processing Research Group, School of Electrical and Electronic Engineering, University of Manchester, as a Research Associate. In 2018, he was appointed as a Lecturer in Embedded Systems with The University of Manchester. His research interests include the development of electromagnetic sensor systems for security, landmine detection, and polar sensing.

John L. Davidson received the B.Sc. (Hons.) degree in engineering physics and the Ph.D. degree in Mössbauer spectroscopy from Sheffield Hallam University, Sheffield, U.K., in 1993 and 1997, respectively.

As a Research Fellow at the University of Southampton, Southampton, U.K, from 1998 to 2002, he developed an interest in electrostatics and electromagnetics. In 2002, he joined The University of Manchester, Manchester, U.K., initially working in the area of electrical impedance tomography applied to industrial and medical problems and, more recently, in the area of electromagnetics. He has authored and co-authored more than 40 scientific publications. His research interests include electromagnetic modeling, inverse problems, and magnetic induction sensor development.

Dr. Davidson was awarded the Beloe Fellowship Award from the Worshipful Company of Scientific Instrument Makers in 2008.

Edward Cheadle is a Research Associate with experience in academia and industry in the areas of optical instrumentation and precision mechanics. His research focuses on a novel embedded system utilizing photogrammetry and computer vision for the real-time determination of the position of a handheld electromagnetic detector head.

Frank J. W. Podd was born in Lowestoft, U.K., in 1970. He received the B.Sc. degree in theoretical physics, the M.Sc. degree in pattern recognition and machine learning, and the Ph.D. degree in medical image processing from the University of Surrey, Guildford, U.K., in 1992, 1993, and 1997, respectively.

He has worked in academia and industry, creating scientific instruments, and now teaches embedded systems at The University of Manchester, Manchester, U.K. His research interest is in multi-in–multiout (MIMO) ground-penetrating radar.

Anthony J. Peyton received the B.Sc. degree in electrical engineering and electronics and the Ph.D. degree in medical instrumentation from The University of Manchester Institute of Science and Technology (UMIST), Manchester, U.K., in 1983 and 1986, respectively.

After various positions in the scientific instrumentation industry and academia, he was appointed as a Professor in electromagnetic engineering from The University of Manchester, Manchester, in May 2004. He has over 30 years of experience in a diverse range of electromagnetic sensor systems and has been the principal investigator of numerous national, international, and industry-funded projects. He has also been a partner of many major EU projects. He has co-authored almost 140 international journal articles related to electromagnetics and sensing. His group works extensively with industry, taking electromagnetic sensors from fundamental research in the laboratory through to final applications in a range of real-world settings, from detecting meteorites in the Antarctic, to steel mills around the world and nuclear reactors in the U.K.